Annals of Glaciology 34 2002

A ground-based, multi-frequency ice-penetrating radar system

Kenichi Matsuoka,[1] Hideo Maeno,[2] Seiho Uratsuka,[2] Shuji Fujita,[3] Teruo Furukawa,[4] Okitsugu Watanabe[4]

[1]*Institute of Low Temperature Science, Hokkaido University, Sapporo 060-0819, Japan*
[2]*Communications Research Laboratory, Nukui-kita, Koganei, Tokyo 184-8795, Japan*
[3]*Department of Applied Physics, Graduate School of Engineering, Hokkaido University, Sapporo 060-8628, Japan*
[4]*National Institute of Polar Research, Kaga, Itabashi-ku, Tokyo 173-8515, Japan*

ABSTRACT. To better understand how ice sheets respond to climate,we designed a new multi-frequency ice-penetrating radar system to investigate subsurface structures of ice sheets. The system is mounted on a single platform and handled by a single operator. Three radio frequencies, 30, 60 and 179 MHz, were used. An underlying principle of these multi-frequency observations is that the lower frequencies are more sensitive to electrical conductivity changes, whereas the higher frequencies are more sensitive to dielectric permittivity fluctuations in the ice. The system is composed of three single-frequency pulse radars, a trigger-controller unit and a data-acquisition unit. The trigger controller is the key component of this system. It switches transmitters on at different timings to prevent mixing of signals among the three radars. The timing difference was set as 50 μs, which is equivalent to the two-way travel time for radio waves reflecting from 4250 m below the surface. A field test was done along a 2000 km long traverse line in east Dronning Maud Land, Antarctica. The multi-frequency system successfully acquired data that are equivalent in quality to our earlier single-frequency measurements along the same traverse line. The details of the system and preliminary data are described.

INTRODUCTION

To understand the role of ice sheets in the climate system, the physical properties in the ice must become better known. For instance, there are significant variations in ice density, crystal orientation and size, and electrical conductivity that can be used to infer past climate and help to explain present ice movements. Remote sensing is a practical approach to measuring ice properties over large areas. In particular, ice-penetrating radar is a powerful tool for observing the internal properties of ice masses (e.g. Robin and others, 1969; Bogorodsky and others, 1985). Electromagnetic waves at frequencies between a few megahertz and a few gigahertz can be used in ice-sounding radars. Radio waves reflect off surfaces where there is a contrast in either the dielectric permittivity or electrical conductivity. Such contrasts occur not only at the surface and base of the ice sheet, but also within the ice.

There are three known causes of internal reflections of ice sheets: changes in dielectric permittivity due to density fluctuations (e.g. Paren and Robin, 1975; Clough, 1977), changes in dielectric permittivity due to changes in crystal-orientation fabrics Δ_{cof} (e.g. Harrison, 1973; Fujita and others, 1993), and changes in electrical conductivity due to acidity changes (e.g. Millar, 1981; Moore, 1988; Moore and Fujita, 1993; Matsuoka and others, 1996). Fujita and Mae (1994) pointed out an essential difference between the conductivity- and permittivity-based reflections. That is, the power reflection coefficient R due to a conductivity change is strongly dependent on radar frequency and ice temperature. In contrast, R due to a permittivity change is virtually independent of either radar frequency or temperature. This is shown quantitatively in Figure 1. For instance, if the frequency triples from 60 to 179 MHz, R drops by a factor of 9 (inverse frequency squared), or equivalently 9.5 dB, if the reflection was due to changes in electrical conductivity. But R would not change at all if the reflection was due to changes in dielectric permittivity. Hence, if we use two frequencies for radar sounding, we can distinguish between conductivity- and permittivity-based reflections. Fujita and others (1999) used 60 and 179 MHz radars in East Antarctica and found that the dominant cause of internal reflection changed with depth and region. The dominant causes of reflection at 60 and 179 MHz are conductivity- and permittivity-based reflections, respectively. However, there is still a significant contribution of permittivity- and conductivity-based reflections at both 60 and 179 MHz. For instance, at 60 MHz, R due to an acidity change at $-25\,^{\circ}$C is comparable to the R due to Δ_{cof} of 20%. Moreover, at 60 MHz, R due to an acidity change at $-50\,^{\circ}$C is smaller than the R due to Δ_{cof} of 10%, which is a typical change of Δ_{cof} in ice sheets. Thus, referring to Figure 1, to ensure that the radar reflection is from fluctuations in conductivity, a frequency of about 10 MHz or less is needed, whereas a frequency of about 300 MHz or more is needed to ensure that the radar reflection is from fluctuations in permittivity. Furthermore, in addition to the two-frequency observation to distinguish permittivity- and conductivity-based reflections, the third frequency would be helpful to see if the data really followed the tendencies shown in Figure 1. Hence, we believe that an appropriate method to understand the substructure of ice sheets is to use several radar frequencies between a few megahertz and a few gigahertz.

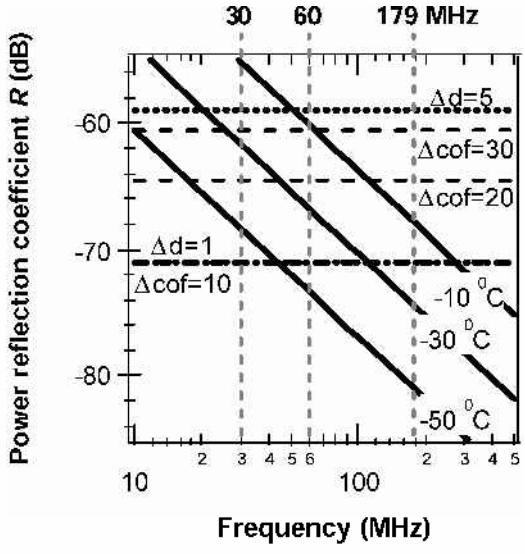

Fig. 1. Predicted frequency dependence of reflectivities R. The signals reflect off regions with permittivity changes due to crystal-orientation fabrics (Δ_{cof} in per cent change of c-axis orientation) (dashed lines), ice-density changes (Δd in kg m^{-3}) (dotted lines), and an electrical conductivity change, which could be due to an acidity change of 10 μmol L^{-1}, at various temperatures (solid lines). R does not depend on the pressure, and R due to permittivity changes does not depend on the ice temperature. Thirty per cent of Δ_{cof} is the realistic maximum, but 10% is typical (Fujita and Mae, 1994). Lines for 10% of Δ_{cof} overlap with $\Delta d = 1.0$ kg m^{-3}. For details of the calculations, see Fujita and Mae (1994) and Fujita and others (2000). Vertical dashed lines show the frequencies used in this study.

However, handling multiple radars is not an easy task for a traverse team. Fujita and others (1999) operated two single-frequency radars at two platforms simultaneously; however, this required them to set up and maintain two entire systems. Moreover, this required an operator for each of the platforms, which were separated by a distance of more than a few hundred meters to prevent interference between the radars. Through this experience, we recognized that it was necessary to construct an improved system specifically designed for the multi-frequency technique. There are many studies on efficient radar instrumentation for glaciology, as summarized by Bogorodsky and others (1985) and Gogineni and others (1998), but there has been no attempt to construct a ground-based multi-frequency system which employs pulse-modulated radars on a single platform.

A new, single-platform, multi-frequency system was designed in 1997, and the first field test was carried out in the 1999/2000 field season by the 40th Japanese Antarctic Research Expedition (JARE). The radar observations were successfully completed for 2 months, and the total surveyed distance was > 2000 km. Because we used 60 and 179 MHz on a previous expedition, we chose to use these frequencies to make comparisons, and add a third frequency. This new frequency was chosen to be 30 MHz because this frequency is more sensitive to changes in acidity. We verified that the quality of new data from our multi-frequency system is equivalent to that of the earlier data obtained from our conventional single-frequency systems. In this paper, we first describe the new multi-frequency radar system. Second, we present a few examples of the preliminary data and a comparison with the earlier data obtained by our conventional single-frequency systems.

MULTI-FREQUENCY RADAR SYSTEM

Overview of the system

Our requirements for the multi-frequency radar sounding system are (i) to mount the whole system on a single platform, (ii) to have a single controller and recording system for all radar frequencies, and (iii) to require only a single operator in a field survey for long periods without significant stress. Therefore, we designed a triggering system and a recording system to control simultaneously multiple single-frequency radars mounted on a single platform. If we consider the development of a unified multi-frequency radar system, a multi-frequency system using wide-band antennas such as log-periodic antennas would be a possible choice. However, we decided to unify not the radars themselves and antennas, but instead the trigger controller and the recording system. An advantage of this choice is that each radar can be used either as a part of a multi-frequency system or as an independent single-frequency radar. In addition, with this system, we can choose the frequencies to fit the scientific objective. This flexibility is necessary because the most appropriate frequencies can depend on the ice-sheet conditions such as temperature, impurity concentrations and the depositional environments, which vary widely by location and depth, and between the Greenland and Antarctic ice sheets.

The main goal of the design is to operate up to three single-frequency radars simultaneously. The system is composed of a trigger controller, a recording system and the radar transmitters and receivers (Fig. 2). The trigger controller and the recording system are common for all radars and are controlled by a personal computer. All instruments except antennas were mounted inside the snow vehicle. The system described below is slightly different from the one we tested, as described later, because we prefer to use the same type of antenna (three-element Yagi) for all frequencies to fit all three radar systems on the same platform.

Triggering and recording units

The trigger controller is the key component of the multi-frequency system. It sends trigger pulses to all radars in the system, but at different timings for each of them (see panels in Fig. 2c). The timing difference for each radar, 50 μs, was equivalent to the two-way travel time of the electromagnetic waves down to an ice depth of about 4250 m. Where ice is thicker than 4250 m, we simply increase the timing difference.

A digital storage oscilloscope and a personal computer were used to record the data. The oscilloscope digitizes and averages the received signals on the logarithm, and sends them to the computer. A software program controlled the oscilloscope, displayed A- and Z-scopes (time series of radar echoes and pseudo-cross-sections of ice sheets for each frequency) and acquired data. The digitized time-step per datum was 20 ns, and the time window was 50 μs; 2500 8-bit digitized values are acquired for a set of received signals.

Three single-frequency radars

Choice of frequencies

To better understand the ice-flow features and the relation between radar echoes and ice-core signals, we added the relatively low frequency of 30 MHz to obtain depth vari-

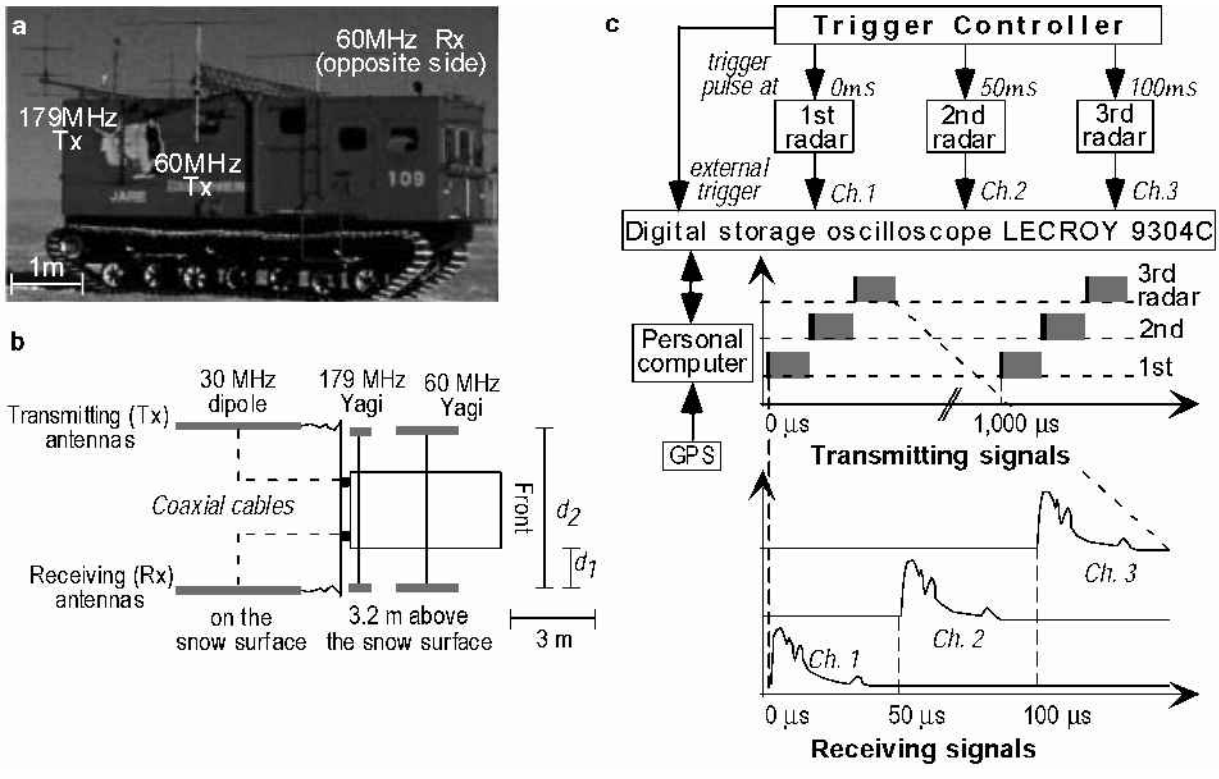

Fig. 2. A ground-based, multi-frequency ice-penetrating radar system. (a) The snow vehicle with attached 60 and 179 MHz three-element Yagi antennas. (b) Top-view schematic of the three-frequency observation system on a single platform. (c) The trigger controller sends a timing signal to the oscilloscope and each radar transmitter in turn. The oscilloscope also receives the reflected radar signals and sends the data to a personal computer through General Purpose Information Bus (GPIB). The computer also collects position coordinates from the global positioning system. A schematic of the transmitted pulse timing (top panel) and received signals (bottom panel) is shown at bottom. The transmitted pulses are the solid black bars; the gray rectangles are the observation time windows. For our tests in the 1999/2000 field season, the 30 MHz radar was mounted on another platform to use three-element Yagi antennas, which is the same type of antenna as the 60 and 179 MHz systems, and the ports connected to/from the third radar were terminated.

ations of high-acidity layers, because some of them are thought to be isochrones. As shown in Figure 1, it is clear that R due to acidity changes is much larger than R due to permittivity changes at even lower frequencies, such as 10 MHz; however, an antenna for such a frequency would be too large and would require a longer pulse width, which has poorer vertical resolution in the ice. Generally speaking, if the frequency triples from 10 MHz to 30 MHz, the antenna dimension and the vertical resolution are to be one-third. On the other hand, at 30 MHz, the R due to acidity changes is 6 dB larger than at 60 MHz. In consequence, we consider that 30 MHz is the realistic lowest frequency for ground-based pulse radar operation to distinguish echoes arising from acidity changes from other processes.

Specifications of the radars

Specifications of the three pulse radars are shown in Table 1. Each radar can be disconnected from the multi-frequency system and used independently. Of these three radars, the 30 MHz radar was newly developed for this study, the 60 MHz radar was modified from the radar used in JARE 37 (Fujita and others, 1999), and the 179 MHz radar was also modified from the radar used in JARE 27, 33 and 37 (Maeno and others, 1994; Uratsuka and others, 1996; Fujita and others, 1999). The major improvements for the latter two radars are the addition of an external trigger port to be controlled by the trigger controller (Fig. 2c) and of the pulse width of 0.5 µs, so that it matches the highest resolution of the 30 MHz radar. Figure 2a and b show how the antennas were arranged on

Table 1. Specifications of three single-frequency radars

	Carrier frequency		
	30 MHz	60 MHz	179 MHz
Transmitter			
Peak power (kW)	1	1	1
Pulse width (µs)*	0.5/1.0	0.25/0.5/1.0	0.06/0.25/0.5/1.0
Repetition rate (kHz)	1.0	1.0	1.0
Receiver			
Sensitivity (dBm)†	−115	−105	−110/−115/−115/−120
Dynamic range (dB)	70	80	80/80/80/85
Bandwidth (MHz)	2.4	4.0	14.0/4.0/4.0/2.0*
Time window (µs)	50 (equivalent depth: 4250 m**)		
Antenna			
Type	Two sets (transmitting/receiving) of three elements Yagi		
Gain (dBi)‡	7.0	7.2	8.25
Total power consumption (W)	100.8	336	36
Wavelength in ice (m)**	5.6	2.8	0.94
Vertical resolution in ice (m)**	42/84	21/42/84	5/21/42/84

* Pulse widths are selectable and bandwidth adjusts automatically depending on the pulse width at 179 MHz.

† dBm is a unit for expression of power level in decibels with reference to a power of 1 mW.

‡ dBi is a unit for expression of antenna gain in decibels with reference to a power of an ideal isotropic antenna.

** Permittivity is assumed as 3.15, and vertical resolution is the inverse of the pulse width.

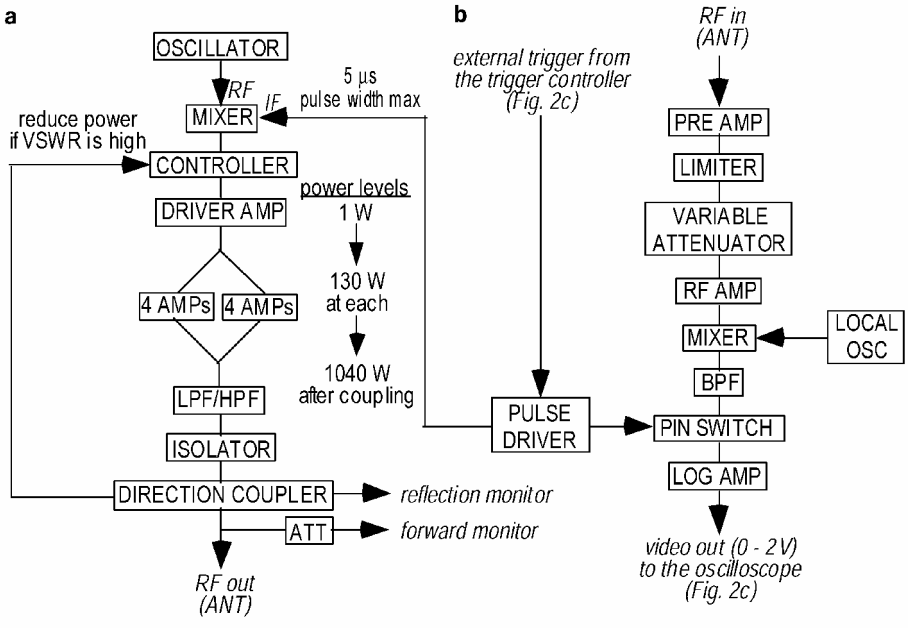

Fig. 3. Block component diagrams of transmitter (a) and receiver (b). (a) The oscillator generates the radio frequency (RF) signal, and the double-balanced mixer modulates the RF with a pulse (IF). After the driver amplifier, the power is amplified with eight amplifiers that are connected in parallel. Power levels given in (a) are output levels of the amplifier(s). LPF, HPF and BPF represent low-, high- and bandpass filters, respectively. The isolator and direction coupler work to protect other components from the reflection power from the transmitting antennas. (b) The reflected signal from the antenna goes first to the pre-amp. The limiter and attenuator decrease the large received signals from snow surface and the transmitting antenna directly. A pin switch opens the observation windows according to the timing from the pulse driver. A log amplifier detects received signals.

the snow vehicle. To compare radar echoes from different frequencies simply, we used the same pulse width (mainly 0.5 μs) and the same type of antennas (three-element Yagi) for all frequencies.

Transmitter and receiver

Figure 3 shows the simplified block diagrams of the transmitter and the receiver of the 30 MHz radar. The transmitter generates a 1040 W pulse according to the external triggering from the trigger controller. The receiving gate is also switched on by the trigger controller and has been opened until the delay time of 50 μs. Through the log-amplifier, received signals from the antennas are transformed to the recorder on a logarithmic scale. To protect internal components, the transmitter has self-guard circuits. When the voltage standing wave ratio (VSWR) is high, the controller reduces the power level. If the pulse driver produces a pulse that is too long, the transmitters are automatically shut off (see Fig. 3a). The architecture of the 179 MHz and 60 MHz radars is similar.

Antennas

The transmitting and receiving antennas for each frequency are set at opposite sides of the vehicle, as shown in Figure 2a. Figure 2a is a photograph of the snow vehicle, which has the 60 and 179 MHz antennas. Table 2 provides some of the dimensions (e.g. the antennas were 3.2 m above the snow and 1.5–2.5 m away from the side of the vehicle). Thus, the radiation pattern and the gain must be coupled with the snow surface and the vehicle. As a result, the input impedance is slightly different from the designed value (50 Ω), and the actual VSWR is larger (Table 2). Hence, the real antenna gain in the field can be different from the values given in Table 1, which were measured without coupling with the surrounding environment. However, because antennas are always fixed at the same position and the antenna height is the same throughout our field measurements, the gain should be a constant value throughout our experiment. We found no indication of interference between antennas from different radars.

Although the polarization can be adjusted to different directions, we maintained the plane of transmitting and receiving antennas parallel to the vehicles during the traverse observations.

Precautions for deployment under severe conditions

Special care was taken to protect the system from rough handling and harsh temperature conditions. Vibrations from the vehicle's diesel engine and the jolts from the hard, irregular snow surface, vibration and shock of vehicles are unavoidable problems in a ground-based survey. Hence, the system was designed completely with solid-state components. The data storage in the computer had solid-state drives (ADTX model AX-SSD series), which can handle large shocks up to 3000 G.

The low air temperatures, and the large temperature gradients between inside and outside also required special care. Antennas were the only instruments exposed to the outside air. The antennas and the radar were connected by coaxial cables. The coaxial cables are exposed typically to −50°C on one side and room temperature on the other side. Thus, we used a special type of Teflon-based coaxial cable designed for use under a wide temperature range between −65° and 125°C (Junkousha Junflon microwave coaxial cable model DGM060). All connectors mounted on the side of the vehicle were sealed to avoid frost formation.

TEST OPERATION AND PRELIMINARY DATA

Experimental conditions

Although we could have mounted all the radars on a single

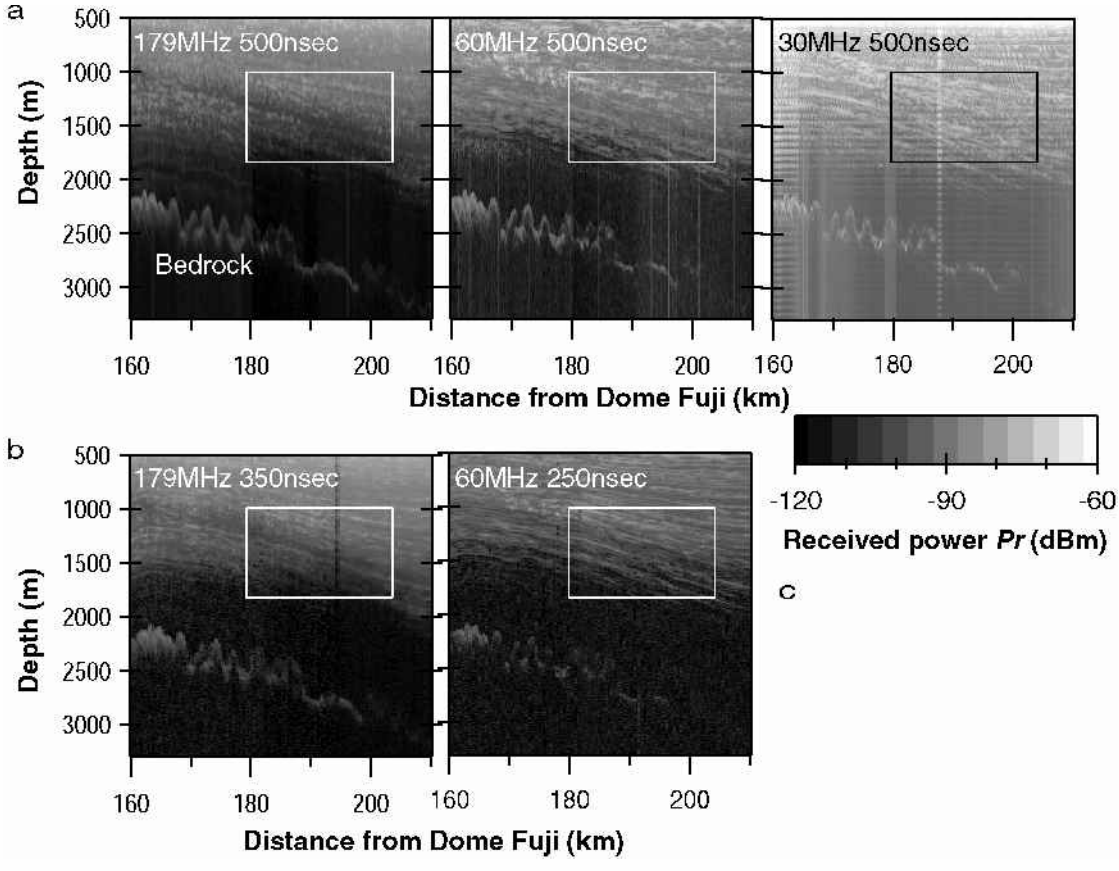

Fig. 4. Examples of a dataset compiled along the main flowline from Dome Fuji, East Antarctica. (a) Data from the present study. The 60 and 179 MHz radars were synchronized as in Figure 2c. The 30 MHz radar was operated independently from a separate platform. Periodic signals in the columns of 30 MHz, typically shown between 160 and 165 km, are noise. (b) Data on the same traverse, but from a previous study without the multi-frequency system (Fujita and others, 1999). For (a) and (b), the abscissa positions of 160 and 210 km are distances from Dome Fuji; the 160 km location is 75°53′ S, 41°18′ E (3690 m a.s.l.); the 210 km location is 75°27′ S, 41°47′ E (3640 m a.s.l.). Rectangles are aids to see typical features. (c) Map of Antarctica showing the surveyed traverses in this study (gray lines).

platform, we used only the two radars (60 and 179 MHz) under the multi-frequency system on a single platform. Because of its large size, the three-element Yagi antenna at 30 MHz was put on another platform. Our platform, the snow vehicle, is 2.9 m wide, 6.1 m long and 3.4 m high. If we had chosen the dipole antenna for the 30 MHz observation, we could have mounted all three radars on the platform (see Fig. 2b). However, to obtain a similar radiation pattern for all frequencies and make comparison easier, we used the three-element Yagi antenna for the 30 MHz radar. We were still able to test the multi-frequency system shown in Figure 2c using the two higher frequencies.

The test was carried out along the traverse line connecting Dome Fuji (77°19′ S, 39°40′ E; 3810 m a.s.l.; ice thickness 3028 m) to the Shirase basin, east Dronning Maud Land (Fig. 4c). The total length of the traverse line was >2000 km. For all observations along the traverse, 256-stacked time series of the received signals were obtained. Depending on the speed of the vehicle (4–12 km h^{-1}), a set of received signals contained information averaged over a distance between 30 and 100 m, since it takes around 30 s to stack 256 data and store them in the computer, due to low-speed digitizing and averaging.

Data quality

The power of the transmitters and the gain of the receivers were frequently checked and calibrated. Variations of the transmitted power were <0.2 dB. Also, by measuring the relation between the power at the antenna connector and the output of the recording system (gain), we found that the possible errors in the received power were <0.7 dB. Additional errors may be caused by possible coupling between the antenna and the snow surface and platform. However, the coupling effect modifies the antenna gain as a constant value since this effect is a function of antenna height and distance to

Table 2. Dimensions of antenna setting and measured characteristics of the antennas

	Frequency		
	30 MHz	60 MHz	179 MHz
Distance to the side of the vehicle d_1 (m)	2.5 (0.25λ)	1.5 (0.3λ)	1.5 (0.9λ)
Distance between transmitting and receiving antennas d_2 (m)	7.9 (0.79λ)	5.9 (1.18λ)	5.9 (3.52λ)
Distance to the snow surface from the driven element (m)	3.2 (0.32λ)	3.2 (0.64λ)	3.2 (1.91λ)
Impedance (Ω)*	59	56	42
VSWR†	1.9	1.1	–

Notes: For all frequencies, three-element Yagi antennas were used. The distances in parentheses show the distances compared to the wavelength λ in the free space for each frequency. d_1 and d_2 are shown in Figure 2b.

* Impedance is measured at each center frequency.

† VSWR is calculated from measured forward and reflection power levels (see Fig. 3a). VSWR of the 179 MHz radar was not measurable in the field due to an instrument limitation.

the platform, which are constant throughout our observations. Considering the values of VSWR in Table 2, the systematic error is smaller than a few dB.

We found no interference between the 60 and 179 MHz radars operated under the multi-frequency system. When the distance between the vehicle and the 30 MHz radar was less than about 100 m, interference sometimes occurred. However, the noise was negligible after stacking since the 30 MHz radar was not synchronized to the 60 and 179 MHz radars.

Three frequency radar signals from a single traverse

Figure 4a shows examples of the Z-scope, where radar pulses are stacked next to each other in a time-dependent manner to represent the pseudo-cross-sections of ice sheets, obtained at three frequencies. Our previous data measured without the multi-frequency system are also shown for comparison (Fig. 4b). Both internal reflections and bedrock topography were detected clearly at all three frequencies. All of the internal layers show similar features of inclination, especially at depths of 1000–1500 m.

For data evaluation, it is important to compare these multi-frequency data to our previous data obtained when the 60 and 179 MHz systems were independent of each other. Although the pulse widths are slightly different, we found no essential difference except for the effect of the pulse width. Comparisons between radar echoes with and without this multi-frequency system (60 and 179 MHz) show that the distribution of the reflection strength is generally the same. Therefore, we conclude that our objective of the multi-frequency system was achieved.

Our newly developed 30 MHz data contain noise due to the internal circuit of the radar. This noise is not related to the multi-frequency system and can be removed by filtering. The images in Figure 4a indicate that the reflectivity is dominantly caused by changes in conductivity; the received power P_r in the boxed region is larger at 60 MHz than at 179 MHz, and largest at 30 MHz (Fujita and Mae, 1994; Matsuoka and others, 1996). For instance, at 190 km and 1500 m depth, P_r at 30, 60 and 179 MHz is about −76, −85 and −102 dBm, respectively. To compensate for the difference of system parameters and the wavelength, values of −12 and −7 dB are added to P_r at 30 and 60 MHz, respectively, and then relative P_r is obtained as −88, −92 and −102 dBm at 30, 60 and 179 MHz, respectively. On the other hand, as shown in Figure 1, if acidity changes cause the reflection, P_r at 30 and 60 MHz is 15.5 or 9.5 dB larger than P_r at 179 MHz. Although it is necessary to examine the possible effects from the antenna coupling and the difference of antenna radiation pattern, observed P_r is in good agreement with this predicted difference at the location. As Fujita and others (1999) pointed out, it is plausible that stress relaxation would cause the absence of crystal-orientation-fabric-based reflections, and then acidity changes are the dominant cause of reflection at the downstream side of the subglacial mountains.

CONCLUDING REMARKS

A multi-frequency ice-penetrating radar system was built and used for ground-based observations along the 2000 km traverse in east Dronning Maud Land, Antarctica. The system was composed of the trigger-controller unit, the recording unit and the multiple single-frequency pulse radars. The system can be used for pulse radar systems at any frequency. Also the radars under the system can be used either as part of the system or as an independent single-frequency radar, depending on scientific objectives and logistics limitation. For the test operation, the 60 and 179 MHz radars were synchronized, and a newly built 30 MHz radar was used separately. The pseudo-cross-sections obtained with this system were consistent with predictions and with previous results.

Two important advantages accrue from these results. One is that the entire dataset along the 2000 km long traverse covered by the three frequency measurements can be analyzed similarly. The other is that, by choosing appropriate frequencies in this system, we can fit it to the specific objectives. Our system is simple, yet we believe it can significantly contribute to the understanding of the physics of large ice masses.

ACKNOWLEDGEMENTS

The authors thank all members of JARE 40 (leaders: K. Shiraishi and H. Miyaoka), particularly K. Maegawa, M. Masuda and M. Tutumi, and the traverse team of T. Suzuki, S. Ootani, H. Kameya, K. Yasugahira and N. Endoh.

REFERENCES

Bogorodsky, V.V., C. R. Bentley and P. E. Gudmandsen. 1985. *Radioglaciology*. Dordrecht, etc., D. Reidel Publishing Co.

Clough, J.W. 1977. Radio-echo sounding: reflections from internal layers in ice sheets. *J. Glaciol.*, **18**(78), 3–14.

Fujita, S. and S. Mae. 1994. Causes and nature of ice-sheet radio-echo internal reflections estimated from the dielectric properties of ice. *Ann. Glaciol.*, **20**, 80–86.

Fujita, S., S. Mae and T. Matsuoka. 1993. Dielectric anisotropy in ice Ih at 9.7 GHz. *Ann. Glaciol.*, **17**, 276–280.

Fujita, S. *and 6 others*. 1999. Nature of radio-echo layering in the Antarctic ice sheet detected by a two-frequency experiment. *J. Geophys. Res.*, **104**(B6), 13,013–13,024.

Fujita, S., T. Matsuoka, T. Ishida, K. Matsuoka and S. Mae. 2000. A summary of the complex dielectric permittivity of ice in the megahertz range and its applications for radar sounding of polar ice sheets. *In* Hondoh, T., *ed. Physics of ice core records*. Sapporo, Hokkaido University Press, 185–212.

Gogineni, S., T. Chuah, C. Allen, K. Jezek and R. K. Moore. 1998. An improved coherent radar depth sounder. *J. Glaciol.*, **44**(148), 659–669.

Harrison, C. H. 1973. Radio echo sounding of horizontal layers in ice. *J. Glaciol.*, **12**(66), 383–397.

Maeno, H. *and 7 others*. 1994. Using a mobile radio echo sounder to measure bedrock topography in east Queen Maud Land, Antarctica. *Proc. NIPR Symp. Polar Meteorol. Glaciol.* 8, 149–160.

Matsuoka, K., S. Fujita, T. Matsuoka, T. Ishida, T. Hondoh and S. Mae. 1996. Measurement of the complex permittivity of acid-doped ice from 1 kHz to 30 MHz — new data set for developing ice radar and dielectric analysis of ice cores. *Proc. NIPR Symp. Polar Meteorol. Glaciol.* 10, 25–35.

Millar, D. H. M. 1981. Radio-echo layering in polar ice sheets and past volcanic activity. *Nature*, **292**(5822), 441–443.

Moore, J. C. 1988. Dielectric variability of a 130 m Antarctic ice core: implications for radar sounding. *Ann. Glaciol.*, **11**, 95–99.

Moore, J. C. and S. Fujita. 1993. Dielectric properties of ice containing acid and salt impurity at microwave and low frequencies. *J. Geophys. Res.*, **98**(B6), 9769–9780.

Paren, J. G. and G. de Q. Robin. 1975. Internal reflections in polar ice sheets. *J. Glaciol.*, **14**(71), 251–259.

Robin, G. de Q., S. Evans and J. T. Bailey. 1969. Interpretation of radio echo sounding in polar ice sheets. *Philos. Trans. R. Soc. London, Ser. A*, **265**(1166), 437–505.

Uratsuka, S., F. Nishio and S. Mae. 1996. Internal and basal ice changes near grounding line derived from radio-echo sounding. *J. Glaciol.*, **42**(140), 103–109.